Evaluation of the Dynamic Magnetic Field Induced Effects on the Lattice Loading Efficiency of a Spaceborne Sr Optical Lattice Clock

Jiajun Jing(景加骏)[1,2,*], Yong Shen(沈咏)[1,2,*], Xiaokang Tang(唐骁康)[1,2], Shaolong Zuo(左少龙)[1,2], Yongzhuang Zhou(周勇壮)[1,2], Zhijiao Deng(邓志娇)[1,2], Hong Chang(常宏)[4†] and Hongxin Zou(邹宏新)[1,2,3‡]

[1]College of Science, National University of Defense Technology, Changsha 410073, Hunan, China

[2]Hunan Key Laboratory of Mechanism and Technology of Quantum Information, Changsha 410073, Hunan, China

[3]National Key Laboratory for Positioning, Navigation and Timing Technology, Changsha 410073, Hunan, China

[4]CAS Key Laboratory of Time and Frequency Primary Standards, National Time Service Center, Xi'an 710600, China

2026 年 8 月 16 日

Abstract

We evaluate the effects of the dynamic magnetic field on the lattice-loading efficiency of a spaceborne Sr optical lattice clock. The orbital magnetic field is calculated using the International Geomagnetic Reference Field-14 model and calibrated with in situ MAG-13 magnetometer data to include quasi-static stray fields from onboard electrical equipment. An ensemble Monte Carlo simulation is then employed to systematically investigate the dependencies of the final ensemble-averaged atomic temperature and the optical lattice loading efficiency on the laser saturation parameter s and detuning δ. Feedforward Helmholtz coil compensation based on the IGRF-14 calibrated field prediction restores the time-averaged efficiency from $\bar{\eta} = 5.67\%$ in the uncompensated case to $\bar{\eta} = 13.05\%$. These results quantify the influence of dynamic magnetic fields on lattice loading and provide guidance for magnetic-field compensation in future spaceborne Sr optical lattice clock missions.

Keywords: Sr optical lattice clock, red MOT, Monte Carlo simulation, lattice loading efficiency

PACS:37.10.-x, 37.10.De, 06.30.Ft, 32.60.+i, 02.50.Ng, 07.55.Ge

*These authors contributed equally to this work.

†Corresponding author. E-mail: changhong@ntsc.ac.cn

‡Corresponding author. E-mail: hxzou@nudt.edu.cn

1. Introduction

Optical lattice clocks have achieved a total fractional systematic uncertainty of 8×10^{-19} [1] and a fractional frequency instability as low as 2.9×10^{-19} at an averaging time of $\tau = 20000\,s$ [2]. Deploying such clocks in orbit would combine their high-precision frequency measurement capability with the microgravity environment and global coverage of space platforms, thereby opening new opportunities for relativistic geodesy, tests of fundamental physics, and global timescale dissemination [3–6]. Motivated by these prospects, several space-clock programmes have been initiated, including ESA's Space Optical Clock project [7,8], NASA's Fundamental Physics with an Optical Clock Orbiting in Space mission [9], and the Sr optical lattice clock deployed aboard the China Space Station (CSS) Mengtian module in October 2022, which achieved a fractional frequency stability of 5×10^{-17} [10].

Operating in low Earth orbit at 400 km altitude introduces a challenge absent in ground-based laboratories. As the CSS completes one orbit, the geomagnetic field varies continuously in both magnitude and direction [11,12]. Superimposed on this orbital geomagnetic field is a quasi-static stray field from onboard electrical equipment. Together, these components continuously displace the MOT zero-field point from the trap center, degrading the spatial overlap between the cold atomic cloud and the optical lattice and reducing the lattice loading efficiency [13,14]—a critical parameter directly determining the atom number and, consequently, the quantum projection noise floor of the clock.

In this work, we quantitatively evaluate the effects of a dynamic magnetic field on the lattice-loading efficiency of a spaceborne Sr optical lattice clock [15,16]. The orbital magnetic field is first calculated using the International Geomagnetic Reference Field-14 (IGRF-14) model [17]. To account for quasi-static stray fields from onboard electrical equipment, the calculated field is calibrated with in situ MAG-13 triaxial magnetometer data measured aboard the CSS. The resulting calibrated magnetic field profile is then incorporated into a red MOT dynamical model and ensemble Monte Carlo simulation for Sr atoms. Using this framework, we first characterize the dependences of the ensemble-averaged temperature and lattice loading efficiency η on the saturation parameter s and the narrowband detuning δ, thereby identifying the optimal parameter combination that maximizes the loading efficiency. The calibrated dynamic magnetic field is then applied to quantify the loading-efficiency degradation caused by the magnetic field induced displacement of the MOT zero-field point. Finally, we investigate a feedforward Helmholtz coil compensation strategy based on the calibrated magnetic field prediction, which restores the time-averaged loading efficiency to $\bar{\eta}$=13.05%. These results provide quantitative guidance for magnetic-field compensation in future spaceborne Sr optical lattice clocks.

2. Calculation of the Magnetic Environment Experienced by the Optical Lattice Clock

IGRF is a standard geomagnetic field model compiled and maintained by the V-MOD Working Group of the International Association of Geomagnetism and Aeronomy (IAGA) [18–20]. Each edition of the

IGRF is specified by a set of Gauss coefficients, i.e., spherical-harmonic coefficients, which describe the large-scale spatial structure and secular variation of Earth's main magnetic field from 1900 onward. To accurately characterize secular variation, the IGRF coefficients are revised at five-year intervals. The latest edition, IGRF-14, was released in November 2024; it provides a predictive geomagnetic field model for 2025–2030. Within the IGRF framework, the geomagnetic field vector $\vec{B}$ is derived as the negative gradient of a scalar magnetic potential V [18]:

$$\vec{B} = -\nabla V, \tag{1}$$

In source-free regions above the Earth's surface, V satisfies Laplace's equation and can be expanded as a truncated spherical-harmonic series in terms of the Gauss coefficients g_n^m and h_n^m, consistent with Gauss's theory of the geomagnetic field [21]

$$V(r,\theta,\phi,t) = a\sum_{n=1}^{N}\sum_{m=0}^{n}\left(\frac{a}{r}\right)^{n+1}\left[g_n^m(t)\cos(m\phi) + h_n^m(t)\sin(m\phi)\right]P_n^m(\theta), \tag{2}$$

By applying the standard coordinate transformation between the geocentric spherical and Cartesian coordinate systems, the three field components are obtained as

$$\begin{cases} B_{cx} = -B_\theta = \dfrac{1}{r}\dfrac{\partial V}{\partial \theta} = \displaystyle\sum_{n=1}^{N}\left(\frac{a}{r}\right)^{n+2}\sum_{m=0}^{n}\left[g_n^m(t)\cos(m\phi) + h_n^m(t)\sin(m\phi)\right]\frac{\partial P_n^m(\theta)}{\partial\theta}, \\ B_{cy} = B_\phi = \dfrac{1}{r\sin\theta}\dfrac{\partial V}{\partial \phi} = -\dfrac{1}{\sin\theta}\displaystyle\sum_{n=1}^{N}\left(\frac{a}{r}\right)^{n+2}\sum_{m=0}^{n} m\left[g_n^m(t)\sin(m\phi) - h_n^m(t)\cos(m\phi)\right]P_n^m(\theta), \\ B_{cz} = -B_r = \dfrac{\partial V}{\partial r} = -\displaystyle\sum_{n=1}^{N}\left(\frac{a}{r}\right)^{n+2}(n+1)\sum_{m=0}^{n}\left[g_n^m(t)\cos(m\phi) + h_n^m(t)\sin(m\phi)\right]P_n^m(\theta), \end{cases} \tag{3}$$

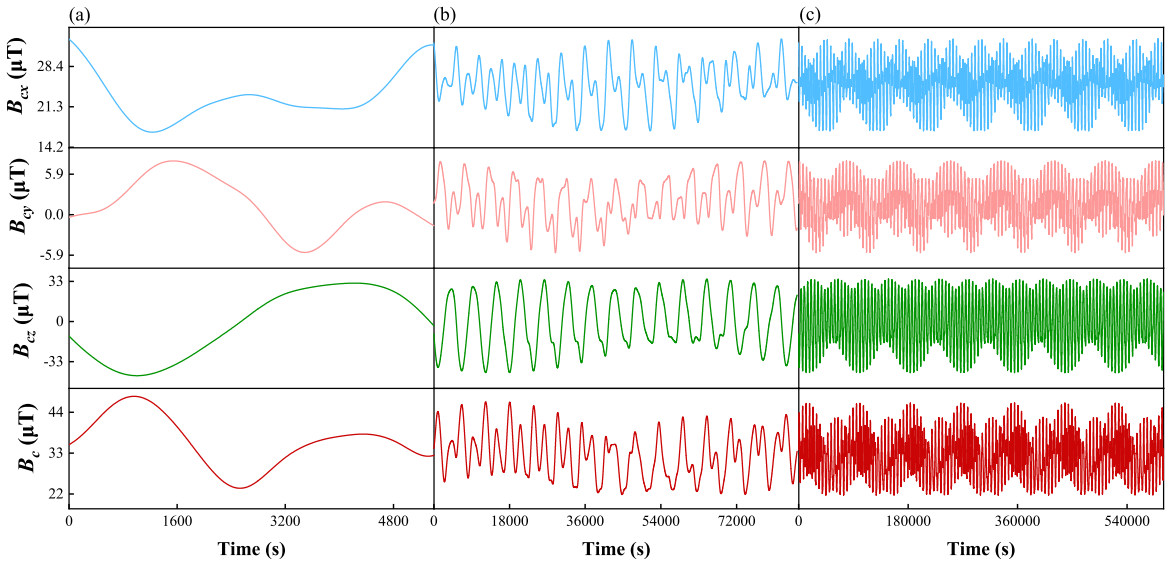


Fig. 1. The time-dependent geomagnetic field along the orbit over one orbital period (a), one day (b), and seven days (c), which are predicted by the IGRF-14 geomagnetic field model. In each panel, the four lines (B_{cx}, B_{cy}, B_{cz}, B_c), from top to bottom, correspond to the northward (x), eastward (y), downward (z) components and the total magnetic field strength, respectively. The horizontal axis denotes time, and the vertical axis represents the strength of the magnetic field.

In the above equations, r, θ, and ϕ denote the geocentric radial distance, geocentric colatitude, and longitude, respectively. a is the reference radius used in the IGRF model. N is the maximum degree of

the spherical-harmonic expansion, and $P_n^m(\theta)$ denotes the Schmidt quasi-normalized associated Legendre function of degree n and order m. The components B_{cx}, B_{cy}, and B_{cz} obtained from Eq. (3) correspond to the northward (x), eastward (y), and downward (z) components of the geomagnetic field, respectively. Once the time and orbital position are specified, the magnetic field along the orbit can be calculated from Eqs. (2) and (3). As shown in Fig. 1, the three components and the total magnetic field exhibit clear periodic variations consistent with the orbital period of the space station.

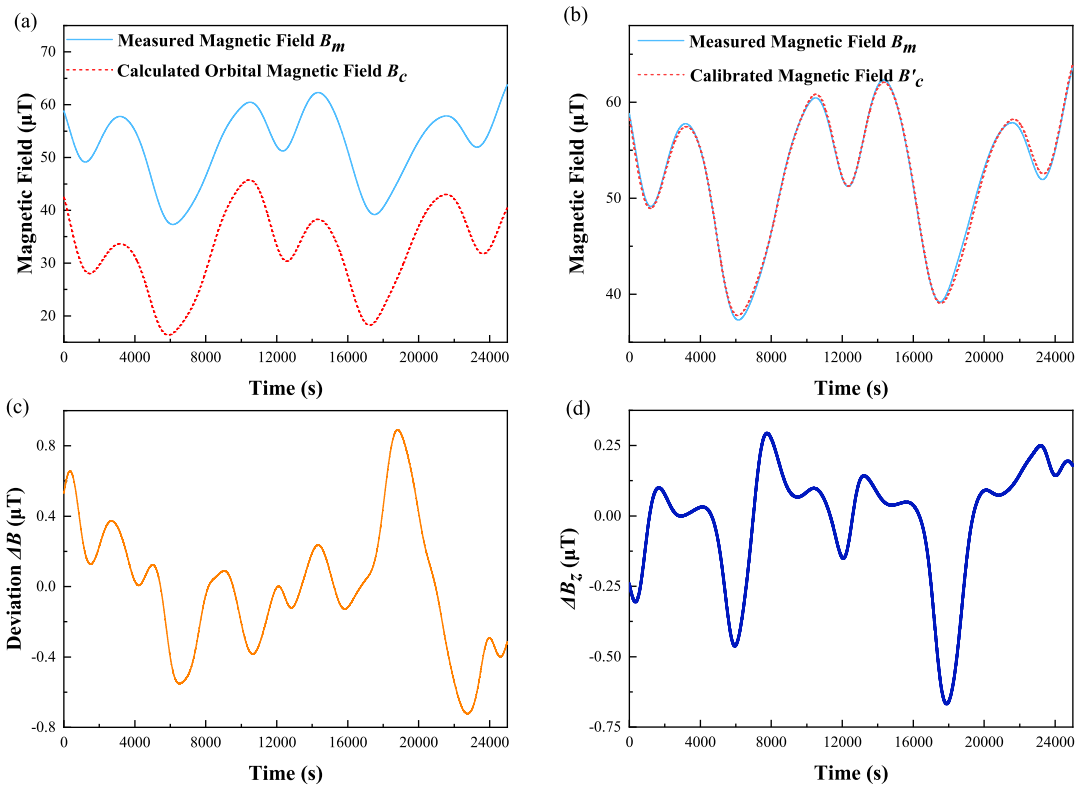


Fig. 2. Comparison of calculated and measured magnetic field values. (a) Calculated orbital field B_c versus onboard MAG-13 magnetometer measurements B_m, showing a constant offset deviation attributable to the quasi-static stray field. (b) Calibrated field B'_c versus B_m after stray field correction, demonstrating close agreement. (c) Residual deviation $\Delta B = B_m - B'_c$ following calibration. (d) Time evolution of the axial deviation ΔB_z, representing the residual axial field that would remain under feedforward compensation based on B'_c.

A MAG-13 triaxial magnetometer was installed near the spaceborne Sr optical lattice clock, and its measurements are transmitted to the ground control center in real time through a space-to-ground satellite link. The coordinate system of the MAG-13 is defined by its mounting orientation on the CSS and is therefore different from the north-east-down (NED) coordinate system used in the IGRF-14 calculation. Using the known orbital trajectory and attitude of the CSS together with the mounting orientation of the MAG-13, the transformation matrix between the two coordinate systems can be determined at each time point. The calculated IGRF-14 magnetic field vector is therefore transformed into the MAG-13 coordinate system before comparison with the magnetometer measurements. According to the Operation and Control Center of the CSS, the electrical equipment inside the module generates a quasi-static magnetic field around the spaceborne Sr optical lattice clock, which results in a constant-term deviation between the calculated values B_c and measurements B_m, as shown in Fig. 2 (a). Once the quasi-static magnetic field is determined, the calculated orbital magnetic field can be calibrated to more accurately represent the

actual magnetic environment experienced by the clock.

We assume the quasi-static magnetic field as a constant vector $\vec{b}$ with components b_x, b_y, and b_z in the magnetometer coordinate system. After adding the corresponding components to the calculated values B^i_{cx}, B^i_{cy}, and B^i_{cz}, the calibrated values B'_c should agree well with the measurements B_m. Based on this, if we can find a set of b_x, b_y, and b_z that minimize the value of the following objective function, we can determine the quasi-static magnetic field.

$$J = \sum_{i=1} \left[(B^i_{cx} + b_x)^2 + (B^i_{cy} + b_y)^2 + (B^i_{cz} + b_z)^2 - (B^i_m)^2 \right]^2, \tag{4}$$

As shown in Fig. 2(b), the calibrated values match the measured values closely. The CSS hull and structural materials may introduce some magnetic shielding and local field distortion. However, since the main structure of the module is made of nonferromagnetic aluminum alloy, its shielding effect on the orbital geomagnetic field is expected to be weak. More importantly, the MAG-13 magnetometer performs in situ measurements inside the CSS and near the optical clock, so the measured magnetic field inherently reflects the local magnetic environment, including possible contributions from the hull, structural materials, and onboard electrical equipment. Therefore, the quasi-static local field contributions reflected in the difference between the IGRF-14 calculation and the MAG-13 measurements are incorporated into the calibrated magnetic field.

Passive magnetic shielding is commonly used in ground-based optical clocks and can effectively suppress environmental magnetic fields. In the present spaceborne system, however, the relatively large openings required for optical access reduce the shielding effectiveness, and the effective shielding factor of the actual shielding structure is difficult to determine accurately [11]. Therefore, the passive shielding effect is not explicitly modeled in the present analysis. Instead, based on the calibrated magnetic field, the subsequent analysis considers feedforward compensation using the active magnetic field compensation coils, which are assumed to generate the prescribed compensation field ideally.

3. Doppler Cooling Dynamics in the Red Magneto Optical Trap Under Microgravity

The atoms used in an optical lattice clock are produced by an effusive oven, which generates a high temperature atomic beam with a broad thermal velocity distribution [22]. The resulting rapid atomic motion introduces several systematic frequency shifts that fundamentally limit measurement accuracy, including the Doppler shift arising from atomic motion and collisional frequency shifts among atoms within the ensemble [23]. Laser cooling is therefore essential to reduce the atomic temperature to the microkelvin regime, thereby effectively suppressing these systematic shifts.

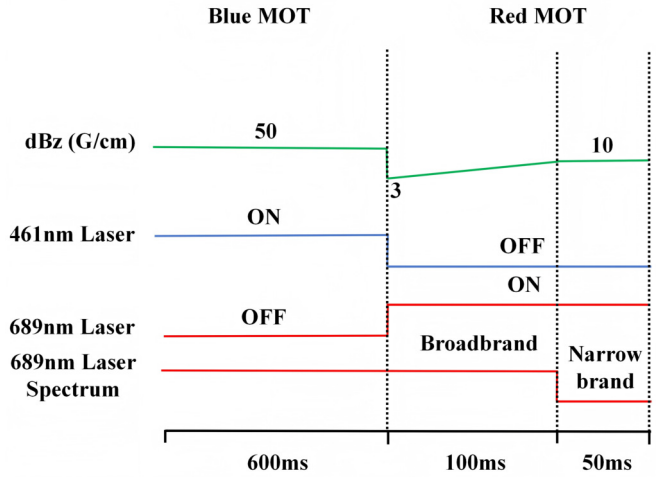


Fig. 3. Timing sequence of the two-stage laser cooling process, showing the time evolutions of the MOT magnetic field gradient (green), the 461 nm blue MOT laser (blue, 600 ms), and the 689 nm red-MOT laser (red). The second stage (red MOT, 150 ms total) consists of an initial broadband phase (100 ms) with a frequency-modulated spectrum for efficient atomic capture, followed by a narrowband phase (50 ms) for final cooling to the microkelvin regime.

The two-stage laser cooling sequence adopted here follows the operational scheme of the spaceborne Sr optical lattice clock. In the first stage, a blue MOT operating on the ${}^1S_0 \rightarrow {}^1P_1$ transition at 461 nm (natural linewidth $\Gamma = 2\pi \times 32$ MHz) [24,25] cools atoms to millikelvin temperatures. In the second stage, the narrow ${}^1S_0 \rightarrow {}^3P_1$ intercombination transition at 689 nm (natural linewidth $\Gamma = 2\pi \times 7.5$ kHz) [26] further cools the atoms to the microkelvin regime. The extremely narrow linewidth of this transition restricts the capture velocity to well below the thermal velocity of atoms leaving the blue MOT; the second stage is therefore implemented in two steps. The 689 nm laser spectrum is first broadened by frequency modulation to a bandwidth of several megahertz to capture the precooled sample efficiently [27], then narrowed to a single frequency for final cooling. Simultaneously, atoms are loaded into a one-dimensional optical lattice operating at the 813 nm magic wavelength [28], where Lamb-Dicke confinement suppresses first-order Doppler broadening and photon-recoil frequency shifts, yielding the well-controlled atomic sample required for clock transition interrogation [29]. The timing sequence of both cooling stages is shown in Fig. 3. For the Sr optical clock on the CSS, the 461 nm blue MOT cooling experiment has been fully realized and quantitatively characterized: CCD imaging successfully captured $(1.50 \pm 0.13) \times 10^6$ Sr atoms within a 1.7 mm atomic cloud [10,30,31]. Based on the foundational blue MOT capability, this work focuses on the influence of dynamic magnetic field on red-MOT cooling and the loading of atoms into the optical lattice.

In the narrow line red MOT under microgravity, axial atomic motion is governed by the scattering force and the residual gravitational acceleration. Focusing on the axial dynamics, the equation of motion for a single Sr atom is [32]

$$F = F_+(v,z) - F_-(v,z) - mg, \tag{5}$$

$$F_\pm(v,z) = \frac{\hbar k \Gamma}{2} \frac{s}{1 + s + \dfrac{4[\delta \mp \vec{k}\cdot\vec{v} \pm \mu \dfrac{dB_z}{dz} z]^2}{\Gamma^2}}, \tag{6}$$

Here $\Gamma = 2\pi \times 7.5\,\text{kHz}$ is the natural linewidth of the ${}^1S_0 \rightarrow {}^3P_1$ intercombination transition, $s = I/I_s$ is the saturation parameter where I is the single beam peak intensity and I_s is the transition saturation intensity, δ is the single beam detuning from resonance, μ is the effective magnetic moment, and $dB_z/dz = 10$ G/cm is the axial magnetic field gradient applied during the narrowband cooling phase. The quantity $g = 4.9 \times 10^{-3}$ m/s^2 is the residual non gravitational acceleration (microgravity level) experienced by atoms aboard the CSS [11].

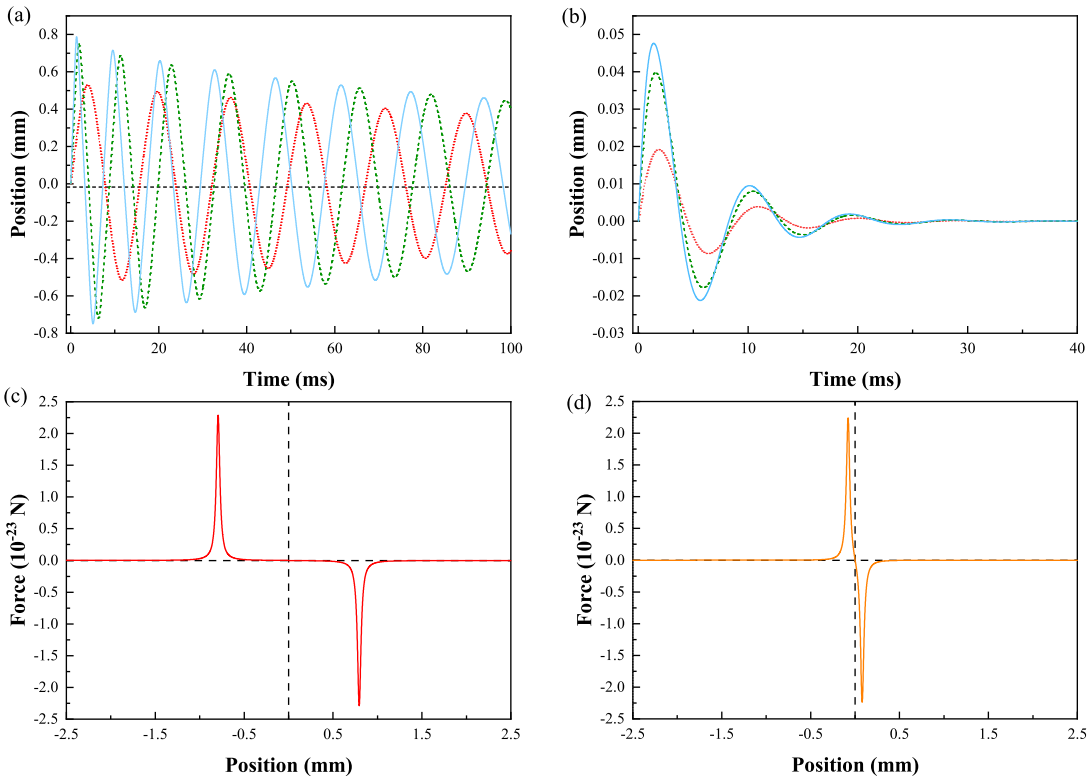


Fig. 4. Simulated axial dynamics of individual Sr atoms in the single frequency red MOT for two laser detuning cases. (a) and (b) Simulated axial trajectories for atoms with initial velocities $v_z(0)$=0.2 m·s^{-1} (blue solid), 0.5 m·s^{-1} (green dashed), and 0.7 m·s^{-1} (red dotted), under large detuning ($\delta = 2\pi\times$-2 MHz) and small detuning ($\delta = 2\pi\times$-200 kHz), respectively. (c) and (d) Spatial profiles of the mean axial MOT force acting on a rest atom ($v = 0$) as a function of axial position, under large detuning ($\delta = 2\pi\times$-2 MHz) and small detuning ($\delta = 2\pi\times$-200 kHz), respectively, demonstrating the broader but weaker restoring force at large detuning compared with the stronger but spatially narrower confinement at small detuning.

Taking the single frequency MOT as an example, the trajectories of atoms with different initial velocities in the MOT are obtained by numerically integrating Eq. (5). In the simulations, all atoms are assumed to originate from the zero-field point of the MOT magnetic field. To illustrate the dependence of the atomic capture range on the laser detuning, simulations are carried out for two cases: large detuning ($\delta = 2\pi\times$-2 MHz) and small detuning ($\delta = 2\pi\times$-200 kHz). The results are shown in Fig. 4.

As shown in Fig. 4, a large laser detuning yields a wider atomic capture range in the MOT but results in significantly weaker cooling performance within the same operating time compared to the small detuning case. This finding explains the necessity of frequency modulating the 689 nm laser during the transition from the blue MOT to the red MOT: the broadened laser spectrum substantially increases the initial capture range of the red MOT, enabling efficient capture of the relatively hot atoms emerging

from the blue MOT, after which the system switches to single frequency operation for final cooling to the microkelvin regime.

4. Monte Carlo Simulation of the Atomic Ensemble

The model presented above considers only the motion of a single atom in the single frequency MOT. As illustrated in Fig. 3, the second stage proceeds through two sequential sub-stages: a broadband phase (100 ms) followed by a narrowband phase (50 ms). In the broadband phase, a sinusoidal frequency modulation at 50 kHz with a depth of 2 MHz is applied to the 689 nm laser [33]. Concurrently, the MOT magnetic field gradient is ramped upward to compress the atomic cloud [34], enhancing the phase space density entering the narrowband phase. In the narrowband phase, the frequency modulation is extinguished, and the detuning is reduced to near resonance. Since the initial positions and velocities of atoms in the red MOT are stochastic, single trajectory calculations cannot yield statistically representative predictions of ensemble-averaged observables such as temperature or lattice loading efficiency.

The present Monte Carlo model is restricted to the axial z direction, which is directly relevant to the displacement of the MOT zero-field position and the spatial overlap between the cooled atomic cloud and the one-dimensional optical lattice. Before entering the blue MOT, the atomic beam is transversely collimated, and the subsequent three-dimensional blue MOT cooling further suppresses transverse motion. Therefore, the one-dimensional model captures the dominant axial dynamics considered in this work. The remaining transverse motion is not assumed to be strictly zero and may introduce a small correction to the absolute loading efficiency, but it is not expected to change the main variation trend associated with the dynamic magnetic field.

Within this one-dimensional framework, statistically representative predictions require propagating a large ensemble of atoms with realistic distributions of initial conditions. The momentum diffusion arising from random recoil kicks during spontaneous emission must also be considered. Here, spontaneous emission is incorporated as a Wiener process, in which the momentum of each atom undergoes Brownian diffusion superimposed on the deterministic semiclassical force. The resulting equation of motion for the i-th atom takes the form [35]

$$m dv_i(t) = F_i[v_i(t), z_i(t)]dt + \sigma[v_i(t), z_i(t)]dw_i(t), \tag{7}$$

where F_i is the semiclassical force from Eq. (5), $dw_i(t)$ is the independent Wiener increment, and the local momentum diffusion coefficient is

$$\sigma[v_i(t), z_i(t)] = \sqrt{\frac{1}{2}\hbar^2 k^2 \gamma[v_i(t), z_i(t)]}, \tag{8}$$

$$\gamma[v_i(t), z_i(t)] = \frac{F_+[v_i(t), z_i(t)] + F_-[v_i(t), z_i(t)]}{\hbar k/2}, \tag{9}$$

The diffusion coefficient in Eq. (8) is proportional to the square root of the local scattering rate, consistent with the fluctuation dissipation relation for two-level atoms in a near-resonant laser field. In the

present ensemble simulation, individual atomic trajectories are propagated independently, and interactions between different atoms are not explicitly included.

For Sr atoms, the atomic temperature at the end of the blue MOT stage is approximately 5 mK [36]. At this temperature, the thermal de Broglie wavelength is far smaller than the spatial extent of the red MOT capture volume [37]; the initial positions $z_i(0)$ are therefore drawn from a uniform distribution spanning the capture range. Each component of the initial velocity $v_i(0)$ is independently sampled from a Gaussian distribution with zero mean and variance $k_B T_0/m$, consistent with a Maxwell–Boltzmann distribution at temperature T_0=5 mK [38], where k_B is the Boltzmann constant and m is the atomic mass of Sr. The ensemble dynamics of atoms through the red MOT cooling sequence are then obtained by numerically integrating Eq. (7).

Successful loading into the optical lattice requires that two selection criteria be jointly satisfied: each atom must remain within the red MOT capture volume throughout the entire cooling sequence, and its kinetic energy at the end of the narrowband phase must not exceed the local lattice potential depth at its final position [39],

$$E_{ki}(z) \leq U(z) = U_0 cos^2(k_{Lat} z), \tag{10}$$

where U_0=60 E_R is the trap depth, defined as the difference between the asymptotic value of the potential and the potential minimum [40]. Fig. 5 displays the simulated trajectories of all atoms satisfying both criteria. Of the simulated atoms, approximately 10.4% satisfy the lattice loading criteria, corresponding to a loading efficiency of $\eta \approx 10.4\%$ ($s = 340$, $\delta = 2\pi\times$-150 kHz).

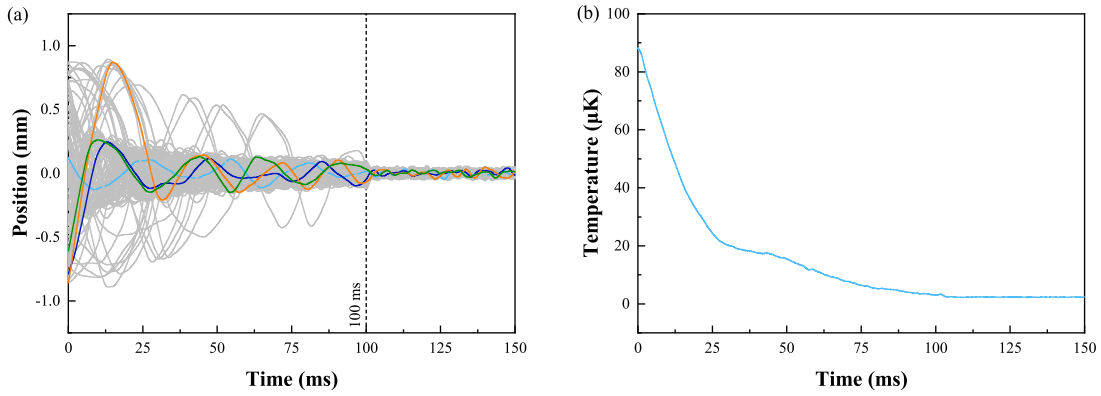


Fig. 5. Monte Carlo simulation of atomic trajectories during the two-stage red MOT cooling sequence for Sr atoms. An ensemble of atoms is propagated with initial positions $z_i(0)$ and velocities $v_i(0)$ drawn from the distributions described in the text; only atoms satisfying both the MOT confinement criterion and the lattice phase space acceptance condition [Eq. (10)] are displayed. Four trajectories are highlighted for clarity. The vertical dashed line at t=100 ms marks the transition from the broadband to the narrowband cooling phase. Panel (a) shows the axial position trajectories; panel (b) shows the evolution of the ensemble temperature throughout the cooling sequence.

According to Refs. [13,41], both the laser saturation parameter s and the detuning δ during the narrowband cooling stage affect the ensemble-averaged atomic temperature at the end of the cooling sequence. Since this temperature directly governs the fraction of atoms satisfying the phase space acceptance criterion of the optical lattice, it consequently influences the lattice loading efficiency. It is therefore necessary to characterize these parameter dependencies under microgravity conditions and identify the

optimal combination of s and δ that maximizes the loading efficiency.

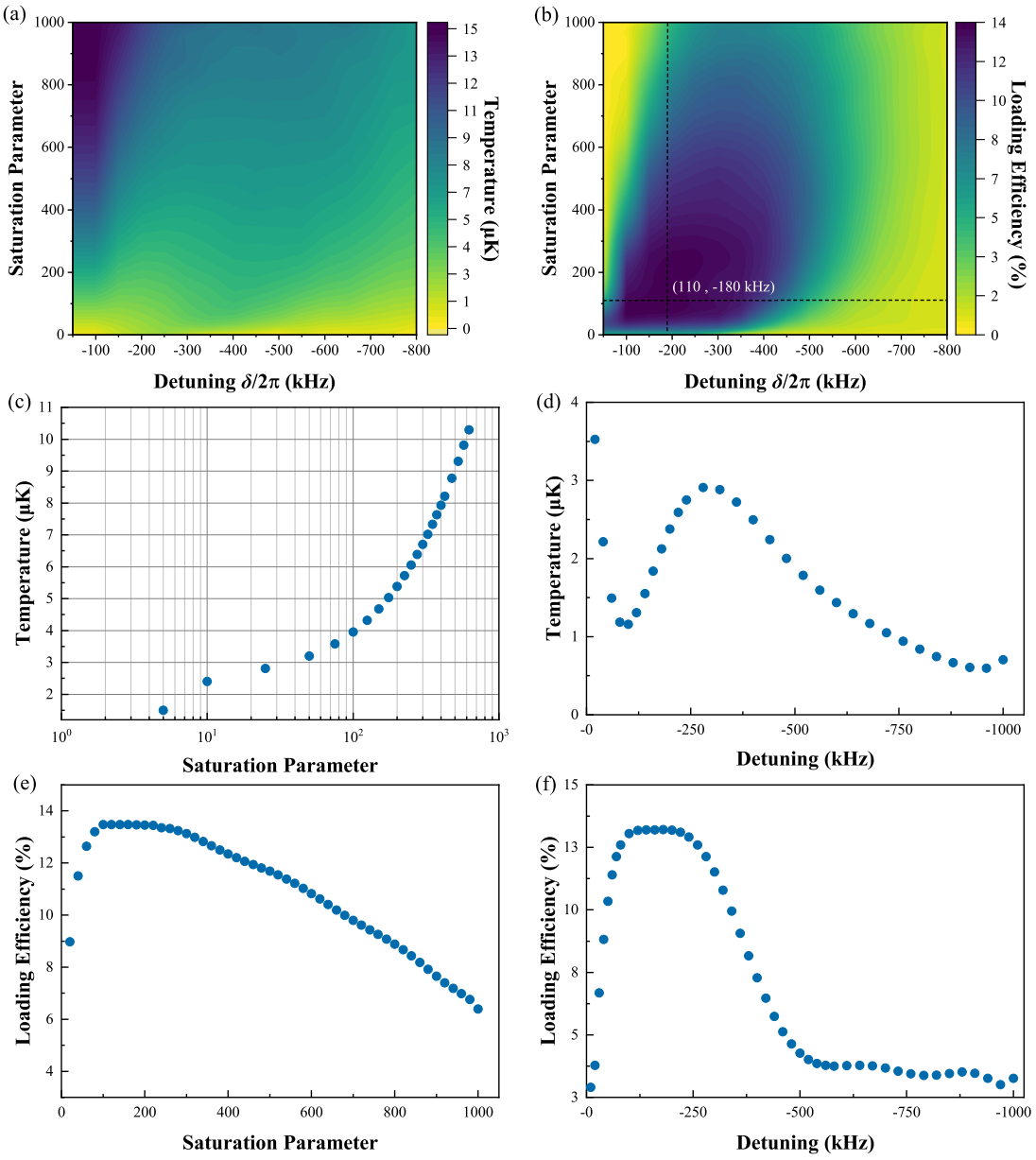


Fig. 6. Dependence of the final ensemble-averaged atomic temperature and lattice loading efficiency on the saturation parameter s and narrowband detuning δ under microgravity conditions. (a) and (b) Two-dimensional distributions of the final ensemble-averaged temperature and lattice loading efficiency in the (s, δ) parameter space, respectively, with a maximum loading efficiency of 13.5% at $(s, \delta) = (110, 2\pi \times -180\ \text{kHz})$. (c) and (e) Ensemble-averaged temperature and lattice loading efficiency as functions of s at $\delta = 2\pi \times -180$ kHz, respectively. (d) and (f) Corresponding quantities as functions of δ at $s = 110$, respectively.

Using the Monte Carlo model established above, we systematically calculate the ensemble-averaged temperature and the lattice loading efficiency over the (s, δ) parameter space, as shown in Figs. 6 (a) and (b), respectively. Fig. 6 (a) shows that, for a fixed detuning, the ensemble-averaged temperature increases nonlinearly and monotonically with increasing s, whereas, for a fixed s, its dependence on δ is nonmonotonic. Because the loading process is jointly governed by the competition between the cooling force and photon recoil heating, the loading efficiency exhibits a nonmonotonic dependence on both s and δ, increasing initially and then decreasing as either parameter is varied. Consequently, Fig. 6 (b) reveals a

unique optimal parameter combination of (s, δ)=(110, $2\pi\times$-180 kHz), at which the lattice loading efficiency reaches a maximum of 13.5%. In practical operation, systematic errors may arise during the setting and adjustment of the laser parameters. Together with external perturbations, these errors make it difficult to maintain s and δ precisely and stably at their optimal combination. We therefore further investigated the individual dependences of the ensemble-averaged atomic temperature and the lattice loading efficiency on each parameter. With the narrowband detuning fixed at $\delta = 2\pi\times$-180 kHz, simulations are performed for multiple values of s over the range [1,1000]. The resulting temperature–saturation parameter and loading efficiency–saturation parameter dependences are shown in Fig. 6(c) and (e), respectively. Complementarily, s is fixed at 110, while δ is varied from $2\pi\times$-1000 to 0 kHz. The corresponding temperature–detuning and loading efficiency–detuning dependences are presented in Fig. 6 (d) and (f), respectively. The results show that the loading efficiency varies gradually in the vicinity of its maximum. Therefore, small systematic deviations of the laser parameters from their optimal values do not lead to an appreciable change in the loading efficiency. These results provide both a methodological reference and quantitative support for determining the acceptable tolerance ranges of laser parameter setting errors in future studies.

5. Dynamic Magnetic Field Induced Loading Efficiency Degradation and Compensation

The dynamic magnetic environment experienced by the spaceborne Sr optical lattice clock is characterized in Sec. 2. The axial component $B_{z,ext}(t)$ of the external field shifts the spatial zero of the MOT field away from its nominal position by a time-dependent displacement $\Delta z(t)$. In a one-dimensional MOT with axial field gradient dB_z/dz, $\Delta z(t)$ is

$$\Delta z(t) = -\frac{B_{z,ext}(t)}{dB_z/dz}, \tag{11}$$

During the narrowband cooling phase, atomic velocities are reduced to near zero, so the Doppler contribution to the scattering force [Eq. (6)] is negligible. The restoring force vanishes at the MOT field zero, and the cooled atomic cloud converges to the position $\Delta z(t)$ rather than to the geometric trap center $z = 0$. This displacement changes the spatial overlap between the atomic cloud and the optical lattice mode, thereby affecting the lattice loading efficiency η.

According to the IGRF-14 model, the magnetic field variation within a single cooling and loading cycle is at the level of 10^{-2} μT, producing a corresponding displacement Δz of only 0.1 μm—entirely negligible compared to the spatial extent of the cold atomic cloud. The external field may therefore be treated as quasi-static over each cycle. To validate this approximation explicitly, we extract the actual magnetic field variation amplitude δB_z experienced by the CSS during a representative orbital segment. As shown in Fig. 7 (a), owing to the extreme brevity of the cooling and loading cycle relative to the orbital period, the dynamic magnetic field undergoes a nearly linear, monotonic variation within the selected time window, with a total amplitude at the level of 10^{-2} μT. This time-varying field profile is then incorporated into the Monte Carlo ensemble simulation in two ways: once with the field evolving continuously according to

the extracted profile, and once with the field held constant at its mean value. As shown in Figs. 7 (b)–(c), the resulting ensemble temperature evolution curves and final atomic position distributions are virtually indistinguishable between the two treatments, with no appreciable difference in cooling performance or lattice loading efficiency. These results confirm that the quasi-static approximation is well justified for the present orbital magnetic environment. The comparison in Figs. 7(b) and 7(c) also shows that the temporal variation of the magnetic field within a single cooling and loading cycle has a negligible influence on the cooling dynamics and the final atomic temperature. Therefore, the dominant effect of the dynamic magnetic environment considered here is the displacement of the MOT zero-field position on the orbital timescale. This displacement changes the spatial overlap between the cooled atomic cloud and the fixed optical lattice mode, thereby causing variations in the lattice loading efficiency.

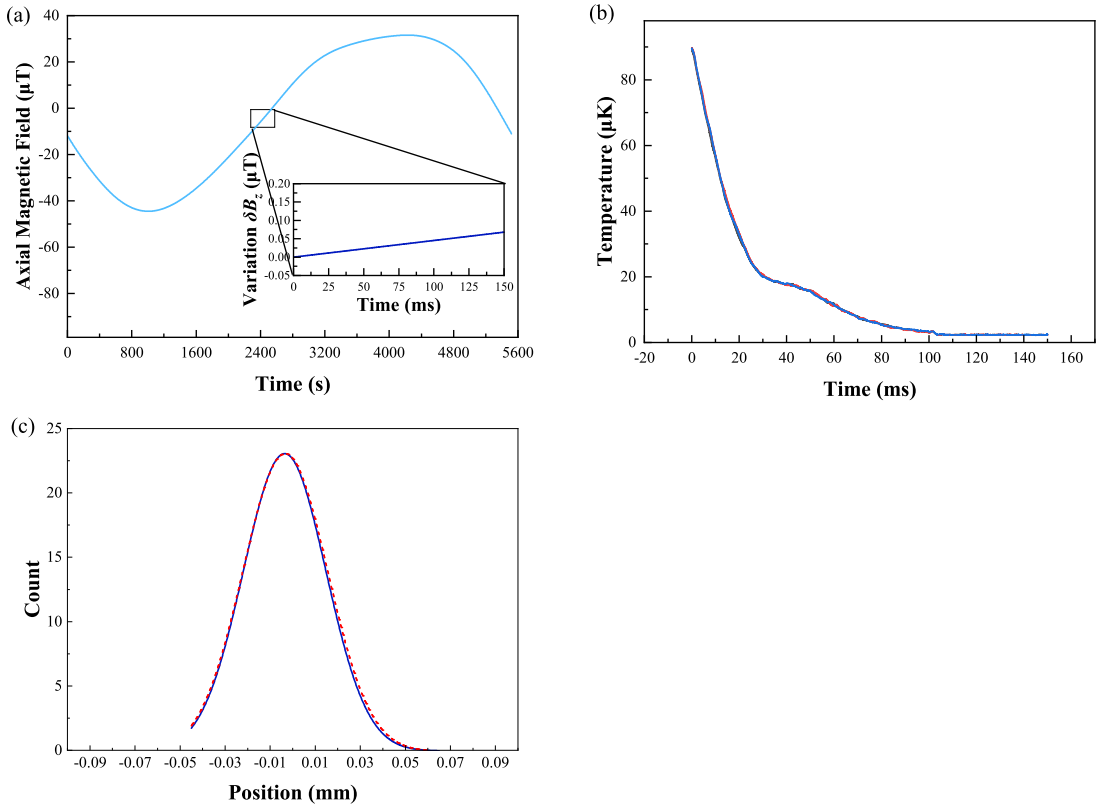


Fig. 7. Validation of the quasi-static approximation using the actual magnetic field variation experienced by the CSS during a representative orbital segment. (a) Time evolution of the axial magnetic field over one orbital period. The inset shows the axial magnetic field variation δB_z during a single cooling and loading cycle, with a total variation at the level of 10^{-2} μT. (b) Ensemble temperature evolution obtained from Monte Carlo simulations using the continuously varying magnetic field profile (blue solid line) and the field held constant at its mean value over the same cycle (red dashed line). (c) Final axial position distributions of successfully loaded atoms for the continuously varying field (blue solid line) and the constant mean field (red dashed line). The close agreement between the two treatments confirms that the external magnetic field can be treated as quasi-static within a single cooling and loading cycle.

Under this approximation, $\eta(t)$ is evaluated for each cooling and loading cycle by substituting the corresponding orbital magnetic field $B_{z,\mathrm{ext}}(t)$ into the Monte Carlo simulation of Sec. 4. The time evolution of $\eta(t)$ under the uncompensated dynamic magnetic field environment is shown in Fig. 8 (a). The loading efficiency exhibits large periodic oscillations correlated with the orbital geomagnetic field variation. The

time-averaged efficiency is $\bar{\eta} = 5.67\%$, representing a reduction of approximately 58% from the simulated optimal value of $\eta = 13.5\%$. This reduction in the time-averaged loading efficiency directly reduces the number of atoms loaded into the optical lattice, increasing quantum projection noise and degrading clock frequency stability.

To restore the lattice loading efficiency, a feedforward compensation strategy is implemented via the Helmholtz coils. The coil currents are calculated from the IGRF-14 calibrated field values B'_{cz} at each epoch. Substituting the resulting field profile into the one-dimensional Monte Carlo simulation yields a time-averaged efficiency of $\bar{\eta} = 13.05\%$, a 130.2% improvement over the uncompensated case. As shown in Fig. 8 (b), however, the compensated efficiency continues to exhibit temporal fluctuations rather than converging to a stable value. The residual variation mainly originates from the deviation between the IGRF-14 calibrated field and the actual magnetic field. This deviation limits the performance of prediction-based feedforward compensation; further improvement may be achieved through active feedback based on real-time magnetometer measurements. Fluctuations in the lattice loading efficiency can affect the clock stability through changes in the number of interrogated atoms. Under the quantum projection noise limit, the frequency instability scales approximately as $N_a^{-1/2}$ [42], where $N_a = \eta N_0$ is the number of atoms loaded into the optical lattice. As shown in Fig. 8(b), the residual fluctuations of η after compensation are small relative to the mean value of $\bar{\eta} = 13.05\%$; therefore, their contribution to the clock instability is expected to be small. In addition, the Sr optical lattice clock employs normalized electron shelving detection, in which the excitation fraction is normalized to the total detected atom number within the same experimental cycle, reducing the sensitivity of the clock readout to cycle-to-cycle atom number variations.

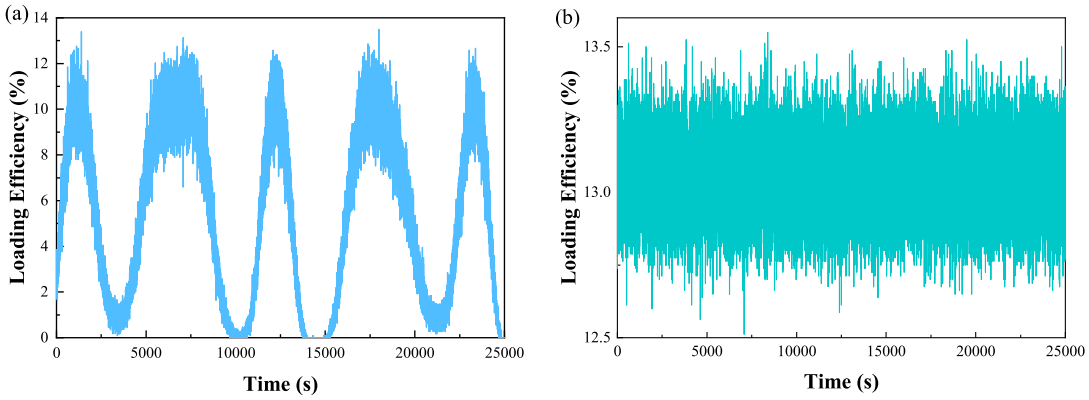


Fig. 8. Simulated lattice loading efficiency $\eta(t)$ of the Sr atoms over the orbital magnetic field profile. (a) Uncompensated case, in which the dynamic external magnetic field shifts the MOT zero-field point and reduces the average loading efficiency to $\bar{\eta} = 5.67\%$. (b) Dynamically compensated case, in which feedforward Helmholtz coil compensation suppresses the residual field and restores the average loading efficiency to $\bar{\eta} = 13.05\%$.

6. Conclusion

We have evaluated the effects of the dynamic magnetic field on the lattice loading efficiency of a spaceborne Sr optical lattice clock. The orbital magnetic field was calculated using the IGRF-14 model and calibrated with in situ MAG-13 magnetometer data to include quasi-static stray fields from onboard

electrical equipment.

Based on the established ensemble Monte Carlo simulation, we systematically investigated the dependencies of the final ensemble-averaged atomic temperature and the optical lattice loading efficiency on the saturation parameter s and detuning δ during the cooling stage. The loading efficiency exhibits a nonmonotonic dependence on both parameters because of the competition among atomic capture, laser cooling, MOT confinement, and photon recoil heating. In the absence of external magnetic perturbations, the maximum lattice loading efficiency reaches 13.5% at s=110 and δ=2$\pi\times$-180 kHz. Moreover, the loading efficiency varies only gradually near this optimum, indicating that the optimized operating point is relatively robust against small deviations in the laser parameters. When the dynamic magnetic field is applied without compensation, the time-averaged efficiency decreases to $\bar{\eta} = 5.67\%$, corresponding to a reduction of approximately 58% from the simulated optimum. This reduction originates from the magnetic field induced displacement of the MOT zero-field point, which decreases the spatial overlap between the cooled atomic cloud and the optical lattice. Feedforward Helmholtz coil compensation using the IGRF-14 calibrated field prediction restores the time-averaged efficiency to $\bar{\eta} = 13.05\%$, corresponding to a 130.2% improvement over the uncompensated case.

Residual fluctuations remain after compensation mainly because of the deviation between the calibrated field prediction and the actual magnetic field. Further improvement may be achieved by active feedback based on real-time magnetometer measurements. The present evaluation quantifies the influence of dynamic magnetic fields on lattice loading and provides practical guidance for magnetic field compensation in future spaceborne Sr optical lattice clock missions.

Acknowledgment

This work was supported by the National Natural Science Foundation of China under Grants 62275268, 62375284 and 62475287, and the Natural Science Foundation of Hunan Province, China (Grant No. 2025JJ20063).

参考文献

[1] Aeppli A, Kim K, Warfield W, Safronova M S and Ye J 2024 *Phys. Rev. Lett.* **133** 023401

[2] Liu X Y, Liu P, Li J, Zhang Y C, Wang Y B, Jia Z P, Zhang X, Zhu X Q, Kong D Q, Song W L, Niu G Z, Yang Y M, Feng P J, Liu X P, Cui X Y, Xu P, Jiang X, Yin J, Liao S K, Peng C Z, Dai H N, Chen Y A and Pan J W 2025 *Phys. Rev. Lett.* **135** 263402

[3] Schiller S, Görlitz A, Nevsky A, Koelemeij J C J, Wicht A, Gill P, Klein H A, Margolis H S, Mileti G, Sterr U, Riehle F, Peik E, Tamm Chr, Ertmer W, Rasel E, Klein V, Salomon C, Tino G M, Lemonde P, Holzwarth R and Hänsch T W 2007 *Nucl. Phys. B-Proc. Suppl.* **166** 300

[4] Chou C W, Hume D B, Rosenband T and Wineland D J 2010 *Science* **329** 1630

[5] Boldbaatar E, Grant D, Choy S, Zaminpardaz S and Holden L 2023 *Sensors* **23** 5998

[6] Camparo J 2023 Applied Atomic Timekeeping in Space, *2023 IEEE/ION Position, Location and Navigation Symposium (PLANS)* 295

[7] Bongs K, Singh Y, Smith L, He W, Kock O, Świerad D, Hughes J, Schiller S, Alighanbari S, Origlia S, Vogt S, Sterr U, Lisdat C, Le Targat R, Lodewyck J, Holleville D, Venon B, Bize S, Barwood G P, Gill P, Hill I R, Ovchinnikov Y B, Poli N, Tino G M, Stuhler J and Kaenders W 2015 *C. R. Phys.* **16** 553

[8] Origlia S, Pramod M S, Schiller S, Singh Y, Bongs K, Schwarz R, Al-Masoudi A, Dörscher S, Herbers S, Häfner S, Sterr U and Lisdat Ch 2018 *Phys. Rev. A* **98** 053443

[9] Cacciapuoti L, Deschenes J D, Newbury N, Sinclair L and Schiller S *Campaign White Paper: Global Time and Frequency Transfer for Clock-Based Fundamental Physics Tests*

[10] Xia J, Wang W H, Zhao G D, Tan W, Zhou Y Z, Guo F, Liu Y, He D J, Feng M, Liang T, Ren J, Meng J W, Shen Y, Lu X T, Lu B Q, Wang Y B, Zhou C H, Zou H X and Chang H 2025 *Rev. Sci. Instrum.* **96** 093201

[11] Ren J, Tan W, Guo F, Liu H and Chang H 2022 *Opt. Precis. Eng.* **30** 1337

[12] Campbell W H 2003 *Introduction to Geomagnetic Fields* (Cambridge: Cambridge University Press)

[13] Katori H, Ido T, Isoya Y and Kuwata-Gonokami M 1999 *Phys. Rev. Lett.* **82** 1116

[14] Xu X Y, Loftus T H, Hall J L, Gallagher A and Ye J 2003 *J. Opt. Soc. Am. B* **20** 968

[15] Loftus T H, Ido T, Boyd M M, Ludlow A D and Ye J 2004 *Phys. Rev. A* **70** 063413

[16] Baillard X, Fouché M, Le Targat R, Westergaard P G, Lecallier A, Le Coq Y, Rovera G D, Bize S and Lemonde P 2007 *Opt. Lett.* **32** 1812

[17] Kerridge D 2007 IAGA, International Association of Geomagnetism and Aeronomy, in *Encyclopedia of Geomagnetism and Paleomagnetism* (Dordrecht: Springer Netherlands) 407

[18] Alken P, Thébault E, Beggan C D and Finlay C C 2021 *Earth Planets Space* **73** 49

[19] Thébault E, Finlay C C, Beggan C D and Alken P 2015 *Earth Planets Space* **67** 79

[20] Chulliat A, Nair M and Califf S 2026 *Earth Planets Space* **78** 26

[21] Heuring F T 1964 *J. Geophys. Res.* **69** 4959

[22] Campbell G K, Ludlow A D, Blatt S, Thomsen J W, Martin M J, de Miranda M H G, Zelevinsky T, Boyd M M, Ye J, Diddams S A, Heavner T P, Parker T E and Jefferts S R 2008 *Metrologia* **45** 539

[23] Band Y B and Vardi A 2006 *Phys. Rev. A* **74** 033807

[24] Takasu Y, Maki K, Komori K, Takano T, Honda K, Kumakura M, Yabuzaki T and Takahashi Y 2003 *Phys. Rev. Lett.* **91** 040404

[25] Takamoto M and Katori H 2003 *Phys. Rev. Lett.* **91** 223001

[26] Zhang G H, Jing J J, Zhang X, Shen Y and Zou H X 2024 *Phys. Rev. A* **110** 053102

[27] Mukaiyama T, Katori H, Ido T, Li Y and Kuwata-Gonokami M 2003 *Phys. Rev. Lett.* **90** 113002

[28] Akatsuka T, Takamoto M and Katori H 2008 *Nat. Phys.* **4** 954

[29] Ludlow A D, Boyd M M, Ye J, Peik E and Schmidt P O 2015 *Rev. Mod. Phys.* **87** 637

[30] Liu Y, Wang W-H, He D-J, Zhou Y-Z, Shen Y and Zou H-X 2023 *Acta Phys. Sin.* **72** 184202

[31] Zhao G D, Xia J, Liu Y, Zhou Y Z and Zou H X 2025 *Chin. Phys. Lett.* **42** 063701

[32] Basdevant J-L and Dalibard J 2019 Laser Cooling and Trapping, in *The Quantum Mechanics Solver: How to Apply Quantum Theory to Modern Physics* (Cham: Springer International Publishing) 199

[33] Sorrentino F, Ferrari G, Poli N, Drullinger R and Tino G 2006 *Mod. Phys. Lett. B* **20** 1287

[34] Zhan C, Ma Z, Wu J T, Li M J, Han C Y, Lu B and Lee C H 2024 *Chin. Opt. Lett.* **22** 080202

[35] Ren J, Liu H, Lu X T and Chang H 2020 *Appl. Sci.* **10** 4928

[36] Chen Y X, Zhou C H, Tan W, Guo F, Zhao G D, Xia J, Meng J W and Chang H 2024 *Appl. Sci.* **14** 1551

[37] Mickelson P G, de Escobar Y N M, Anzel P and DeSalvo B J 2009 *J. Phys. B: At. Mol. Opt. Phys.* **42** 235001

[38] Rowlinson J S 2005 *Mol. Phys.* **103** 2821

[39] Bothwell T 2022 *A Wannier-Stark Optical Lattice Clock With Extended Coherence Times* (Ph.D. Dissertation, University of Colorado Boulder)

[40] Kong D-H, Wang Z-H, Guo F, Zhang Q, Lu X-T, Wang Y-B and Chang H 2020 *Chin. Phys. B* **29** 070602

[41] Boyd M M 2007 *High Precision Spectroscopy of Strontium in an Optical Lattice: Towards a New Standard for Frequency and Time* (Ph.D. Dissertation, University of Colorado Boulder)

[42] Hollberg L, Oates C W, Curtis E A, Ivanov E N, Diddams S A, Udem T, Robinson H G, Bergquist J C, Rafac R J, Itano W M, Drullinger R E and Wineland D J 2001 *IEEE J. Quantum Electron.* **37** 1502